Auger decay of Ar $2p$ satellite states studied with a multielectron coincidence method

M. Nakano,[1,2] Y. Hikosaka,[3] P. Lablanquie,[4,5] F. Penent,[4,5] S.-M. Huttula,[6] I. H. Suzuki,[2] K. Soejima,[3] N. Kouchi,[1] and K. Ito[2]

[1]*Department of Chemistry, Tokyo Institute of Technology, O-okayama, Tokyo 152-8551, Japan*

[2]*Photon Factory, Institute of Materials Structure Science, Oho, Tsukuba 305-0801, Japan*

[3]*Department of Environmental Science, Niigata University, Niigata 950-2181, Japan*

[4]*CNRS, LCPMR (UMR 7614), 11 rue Pierre et Marie Curie, 75231 Paris Cedex 05, France*

[5]*UPMC, Université Paris 06, LCPMR, 11 rue Pierre et Marie Curie, 75231 Paris Cedex 05, France*

[6]*Department of Physics, P.O. Box 3000, 90014 University of Oulu, Finland*

(Received 19 February 2012; published 9 April 2012)

The Auger decay channels of the Ar $2p$ satellite states have been investigated using a multielectron coincidence technique, using a magnetic bottle time-of-flight electron spectrometer. For the $Ar^+(2p^{-1}3p^{-1}np)$ satellite states the $2p$ hole is filled first, while for the $Ar^+(2p^{-1}3s^{-1}4s)$ satellite states the $3s$ hole is filled first with leading to $Ar^{2+}(2p^{-1}3p^{-1})$ states, which subsequently undergo an Auger decay leading to the filling of the $2p$ hole.

DOI: 10.1103/PhysRevA.85.043405 PACS number(s): 32.80.Aa, 32.80.Hd, 32.30.−r

I. INTRODUCTION

Absorption of an x-ray photon by an atom or a molecule leads to the formation of a singly charged ion with a core hole. The formation of such ions is characterized by intense peaks in the photoelectron spectrum. Associated with these peaks, weaker satellite structures can be observed at lower kinetic energies, corresponding to states where the removal of the core electron has been accompanied by the simultaneous excitation of a valence electron to a vacant orbital. These satellite states as well as the main core-hole states usually undergo Auger decay in which an upper-shell electron fills the core-hole accompanied by the emission of an Auger electron. It is interesting to understand how the valence holes and the excited electrons involved in the description of the satellite states affect the Auger decay processes. However, the investigation of the Auger decay of the satellite states is rather limited in conventional Auger electron spectroscopy [1,2], because the cross sections for the formations of satellite states are very small. Moreover, Auger electrons associated with the decay of satellite states can be masked by the Auger electrons originating from the main core-hole states.

Significant progress took place with the introduction by Eland *et al.* [3] of a new magnetic bottle time of flight spectrometer [4], which made it possible to perform photoelectron-Auger electron(s) coincidences with very high efficiency. In this way the Auger decay of satellite states can be clearly isolated [5–8].

In this work we have investigated the Auger decay of Ar $2p$ satellite states using such a spectrometer. The Ar $2p$ satellite states were previously observed by photoelectron spectroscopy [9–12] and threshold photoelectron spectroscopy [13,14], but their Auger decay has not been hitherto reported. Our coincidence method allows us to retrieve the spectra of Auger electrons associated with the satellite states, and to deduce the decay mechanisms of these states. This method has been used previously by us to investigate the Auger decay of Ar $2p$ [15] and $2s$ [16] holes.

II. EXPERIMENTAL DETAILS

Experiments were performed using the undulator beamline BL-16A [17] of the Photon Factory. Single-bunch operation of the storage ring in top-up mode provides a 624 ns repetition period for the 200-ps-width light pulses. Synchrotron radiation is monochromatized by a grazing-incidence monochromator using a varied-line-spacing plane grating. A mechanical chopper consisting in a rotating cylinder (48 000 rpm) with 100 slits was employed to reduce the light repetition rate by admitting one light pulse in every 12.5 μs period into the interaction region of a magnetic bottle electron spectrometer, thus allowing absolute time of flight determination for all electrons [18]. Multiple coincidences were recorded between electrons analyzed in energy by their times of flight in the spectrometer. The detailed description of the spectrometer and of the data acquisition scheme has been given elsewhere [18]. The energy resolving power of the spectrometer $E/\Delta E$ is nearly constant at $\sim$60. The time to energy calibration was performed by measuring Ar $2p$ photoelectron lines at different photon energies, and taking into account correction of the post-collision interaction shift of the photoelectron lines [19,20].

III. THEORETICAL DETAILS

Theoretical intensities of the Auger transitions from $Ar^+(2p^{-1}3s^{-1}4s)$ satellite states to $Ar^{2+}(2p^{-1}3p^{-1})$ states were calculated within the multiconfigurational Dirac-Fock (MCDF) formalism. The GRASP92 code [21] and the RELCI program from the RATIP package [22] were applied. The MCDF method is described in detail elsewhere (see, e.g., Ref. [21] and references therein), so only the main principles are reviewed here. In the MCDF method, the atomic state functions (ASFs) characterized by the total angular momentum J_α and parity P_α are represented in the basis of jj-coupled configuration state functions (CSF) with the same J_α and P_α as $|\Psi_\alpha(P_\alpha J_\alpha)\rangle = \sum_k c_{\alpha k}|\psi_\alpha(P_\alpha J_\alpha)\rangle$. The mixing coefficients $c_{\alpha k}$ are obtained by diagonalizing the two-electron interaction matrix, which allows for electronic correlations to be taken into account. The wave functions are obtained self-consistently using the Dirac-Coulomb Hamiltonian.

In view of the light mass of Ar, the orbital and spin angular momenta of the outer electrons do not strongly interact. Therefore the coupling conditions are close to LSJ coupling. Thus the inherently jj-coupled ASFs were transformed into

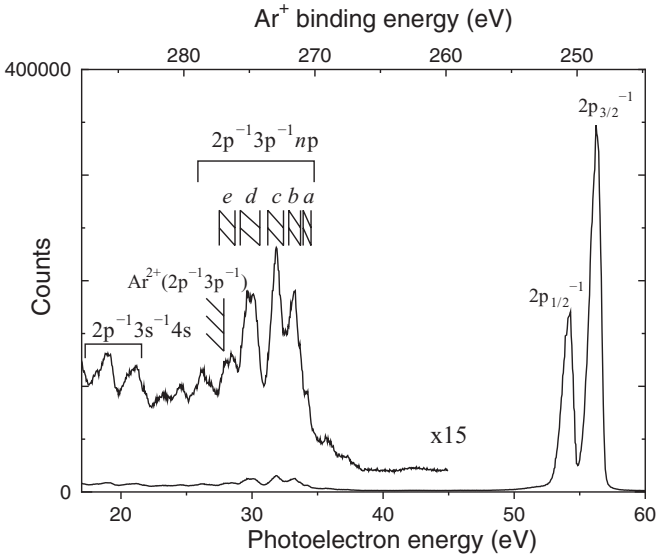

FIG. 1. Photoelectron spectrum of Ar measured at a photon energy of 304.8 eV in the energy range showing the photoelectron peaks for the formation of the $2p$ hole states and the satellite states. The five energy ranges, indicated as a to e, define different groups of $Ar^+(2p^{-1}3p^{-1}np)$ satellite states that will be used to obtain the spectra in Figs. 3, 4, and 5. The core-valence double ionization threshold [16] is shown by the vertical bar with hatches.

the LSJ basis by the unitary transform between the two bases applying the program LSJ [23].

The Auger decay intensity is given by

$$n_{f\beta} = \frac{2\pi \sum_{l_A j_A} \left| \sum_{\mu\nu} c_{f\mu} c_{\beta\nu} M^{\mu\nu}_{f\beta}(J_f J_\beta) \right|^2}{P_\beta(J_\beta)} Q_\beta(J_\beta),$$

where $M^{\mu\nu}_{f\beta}(J_f J_\beta)$ is the Coulomb matrix element

$$\langle \psi_\mu(J_f) \varepsilon_A l_A j_A; J_\beta \left\| \sum_{mn}^{N-1} \frac{1}{r_{mn}} \right\| \psi_\nu(J_\beta) \rangle,$$

$P_\beta(J_\beta)$ is the total decay rate and $Q_\beta(J_\beta)$ is the $|\Psi(J_i)\rangle \rightarrow |\Psi(J_\beta)\rangle$ ionization cross section. The Auger decay intensities were calculated using the AUGER component from the RATIP package. For more details about the AUGER program see Refs. [22,24] and references therein. Channel mixing was omitted in our calculation. When we calculate the Auger transition probabilities, the relative population of $Ar^+(2p^{-1}3s^{-1}4s)$ satellite states is expected to be statistical.

IV. RESULTS AND DISCUSSION

A multi coincidence data set has been accumulated at a photon energy of 304.8 eV. This energy is sufficient to create the $2p$ satellite states with binding energy between 270 and 290 eV [9–14] but is lower than the Ar $2s$ ionization threshold 326.25 eV [25]. Figure 1 shows the photoelectron spectrum of Ar, in the energy range of the $2p$ hole states and the $2p$ satellite states. The two high-intensity peaks around kinetic energy of 55 eV (Ar^+ binding energy of 250 eV) correspond to the $2p_{1/2,3/2}$ hole states with binding energies of 248.628 eV ($2p_{3/2}$) and 250.776 eV ($2p_{1/2}$) [26]. The

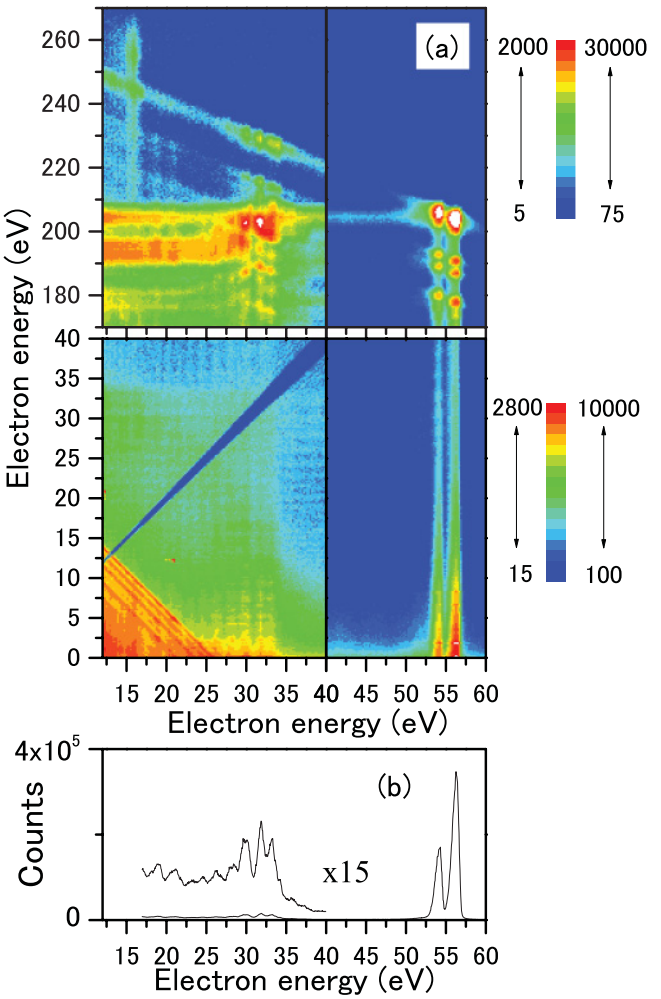

FIG. 2. (Color online) (a) Two-dimensional maps of all coincidence pairs represented as a function of the kinetic energies of two electrons. On the maps, while a process emitting two electrons appears as a single structure, three structures arise from a single process emitting three electrons. For example, formation of the $Ar^+(2p^{-1}3s^{-1}4s)$ satellite states (photoelectron energy of around 20 eV) and the cascade double Auger decay via $Ar^{2+}(2p^{-1}3p^{-1})$ into $Ar^{3+}(3p^{-3})$ (Auger electron energies of 190 and 200 eV) yield two structures which are visible in the range of Fig. 2(a) at (20 eV, ~5 eV) and (20 eV, ~195 eV). Coincidence counts on the maps are plotted on individual logarithm scales. A weak vertical structure seen around (15 eV, 210–270 eV) is associated with the C 1s Auger decay of impurities. (b) The same photoelectron spectrum as in Fig. 1.

associated satellite structures can be observed at higher binding energies. These $2p$ satellite states should have ^2P symmetry—the same symmetry as the $2p$ hole states. The peaks around a binding energy of 275 eV were assigned to the satellite states with the $2p^{-1}3p^{-1}np$ configuration [10,12]. According to the calculation of Dyall *et al.* [10], these peak structures result from the overlap of many $Ar^+(2p^{-1}3p^{-1}np)$ states with $n =$ 4–6: the $Ar^+(2p^{-1}3p^{-1}4p)$ states lie in the binding energy range from 269.9 to 276.6 eV, the $Ar^+(2p^{-1}3p^{-1}5p)$ states from 274.1 to 280.6 eV, and the $Ar^+(2p^{-1}3p^{-1}6p)$ states from 275.8 to 282.2 eV. The five energy ranges, indicated as a to e in Fig. 1, define different groups of Ar^+ satellite states that will be used in Figs. 3, 4, and 5. The $Ar^+(2p^{-1}3p^{-1}np)$ states

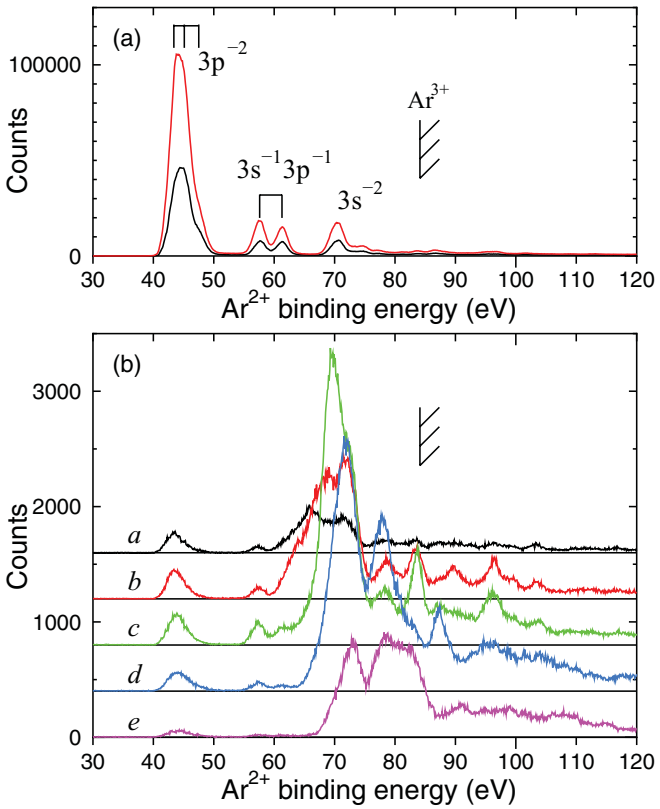

FIG. 3. (Color online) (a) Binding energy of the Ar^{2+} states populated by Auger decay of the $Ar^{+}(2p^{-1})$ states. They are obtained from coincidence events between the photoelectron and Auger electron. The Ar^{2+} binding energy $E_{B^{2+}}$ is deduced from the relation $E_{B^{2+}} = h\nu - (E_{\rm ph} + E_A)$, where $E_{\rm ph}$ is the photoelectron energy and E_A is the Auger electron energy. The L_3MM Auger spectrum associated with the $2p_{3/2}$ decay is shown in red and the L_2MM Auger spectrum associated with the $2p_{1/2}$ decay is in black. The vertical bars indicate the binding energies of $Ar^{2+}(3p^{-2}$: ^3P, ^1D, and $^1S)$ and $Ar^{2+}(3s^{-1}3p^{-1}$: ^3P and $^1P)$ states [28]. (b) Binding energy of the Ar^{2+} states populated by Auger decay of the $Ar^{+}(2p^{-1}3p^{-1}np)$ states. To see easily, each baseline is shifted by 400. The photoelectron energy range set to reduce these Auger spectra are indicated in Fig. 1. The triple ionization threshold (84.124 eV [28]) is shown by the vertical bar with hatches.

in the energy ranges a–c contain only $Ar^{+}(2p^{-1}3p^{-1}4p)$ configuration, that in the d range includes $Ar^{+}(2p^{-1}3p^{-1}4p)$ and $Ar^{+}(2p^{-1}3p^{-1}5p)$ configurations, and that in the e range includes $Ar^{+}(2p^{-1}3p^{-1}np)$ configurations (with $n \geqslant 5$). On the other hand, the two peaks around binding energy 285 eV are assigned to $Ar^{+}(2p^{-1}3s^{-1}4s)$ satellite states, the lower binding energy peak having the $2p^{-1}(^2P_{3/2})3s^{-1}4s$ configuration and the higher one the $2p^{-1}(^2P_{1/2})3s^{-1}4s$ one [11,12]. The $Ar^{+}(2p^{-1}3s^{-1}ns)$ states with $n \geqslant 5$ cannot be distinguished from the background in our spectrum. The conjugate shake-up states, such as $Ar^{+}(2p^{-1}3p^{-1}ns)$ and $Ar^{+}(2p^{-1}3p^{-1}nd)$ states, are not discernible in our spectrum, although they appear in threshold photoelectron spectra [13,14].

Figure 2(a) shows the two-dimensional (2D) maps of all coincidence pairs represented as a function of the kinetic energies of two electrons. Here the horizontal axis is common with the photoelectron spectrum of Fig. 1. Two vertical lines at ∼55 eV associated with $Ar^{+}(2p^{-1})$ photoelectrons indicate the distributions of the Auger electrons emitted in the decay of the $2p$ hole states. The strong islands at $(x, y) =$ (∼55 eV, 170–210 eV) correspond to the dominant single Auger decay of the $2p$ holes. Intensity along the vertical lines is due to the double Auger decay of the holes, and comes from the coincidence of the slower Auger electrons with the $2p$ photoelectrons. In a similar way the Auger decay of the $2p$ satellite states appear in the vertical lines linked to the corresponding photoelectron peaks. Diagonal lines are also seen in Fig. 2(a), and are associated with double photoionization paths: $Ar + h\nu \rightarrow Ar^{2+} + e_{\rm ph1} + e_{\rm ph2}$. In these processes, the available energy, namely the excess of the photon energy compared to the binding energy, is shared by the two photoelectrons. Three diagonal structures with the sum energies of 260, 245, and 235 eV correspond to valence double photoionization processes forming the $Ar^{2+}(3p^{-2})$, $Ar^{2+}(3s^{-1}3p^{-1})$ and $Ar^{2+}(3s^{-2})$ states. The weak and continuous intensity all along these lines shows the direct paths, while the strong island structures on these lines indicate that indirect paths, mediating via Auger decay of the $2p$ hole and $2p$ satellite states, are dominant. The diagonal structures with an energy sum of about 24 eV are associated with core-valence double photoionization processes forming $Ar^{2+}(2p^{-1}3p^{-1})$ states.

A. Auger decay of the $Ar^{+}(2p^{-1}3p^{-1}np)$ states

First, we discuss the single Auger decay from the $Ar^{+}(2p^{-1}3p^{-1}np)$ states. Figures 3(a) and 3(b) show the binding energies of the Ar^{2+} states formed by Auger decay of the $Ar^{+}(2p^{-1})$ and $(2p^{-1}3p^{-1}np)$ states, respectively. They correspond to the intensity distributions along the vertical stripes seen in Fig. 2(a). The $2p$ Auger electron spectra in Fig. 3(a) show the four main peaks originated from the dominant single Auger processes forming $Ar^{2+}(3p^{-2})$, $Ar^{2+}(3s^{-1}3p^{-1})$ and $Ar^{2+}(3s^{-2})$ states [2,15]. In contrast, the Auger spectra of the $Ar^{+}(2p^{-1}3p^{-1}np)$ states, displayed in Fig. 3(b), exhibit weak populations of these Ar^{2+} states, but reveal formation of highly excited Ar^{2+} states with binding energies between 60 and 80 eV. We attribute their formation to spectator decays of the satellite states, and thus the Ar^{2+} final states have the $3p^{-3}np$ configuration. The shapes of these spectator peaks differ from each other, even when comparing the three spectra for the region a–c associated only with the $2p^{-1}3p^{-1}4p$ configuration. This observation implies that the individual initial states arising from different couplings of the electrons in this $(2p^{-1}3p^{-1}4p)$ configuration behave differently in the spectator Auger decay mostly to $3p^{-3}4p$ final states.

The peak at 78 eV, specially enhanced in the spectrum for the d region, which is related to both $Ar^{+}(2p^{-1}3p^{-1}4p)$ and $Ar^{+}(2p^{-1}3p^{-1}5p)$ configurations, suggests that $3p^{-3}5p$ final states are also populated. Below the $Ar^{3+}(3p^{-3})$ thresholds and above the 78 eV peak, we observe formation of Ar^{2+} states which may be associated with spectator decays of the $Ar^{+}(2p^{-1}3p^{-1}np)$ states to $3p^{-3}np$ ($n \geqslant 6$). Furthermore, the peaks above 80 eV may involve spectator decays of the $Ar^{+}(2p^{-1}3p^{-1}np)$ states to $Ar^{2+}(3s^{-1}3p^{-2}np)$ states.

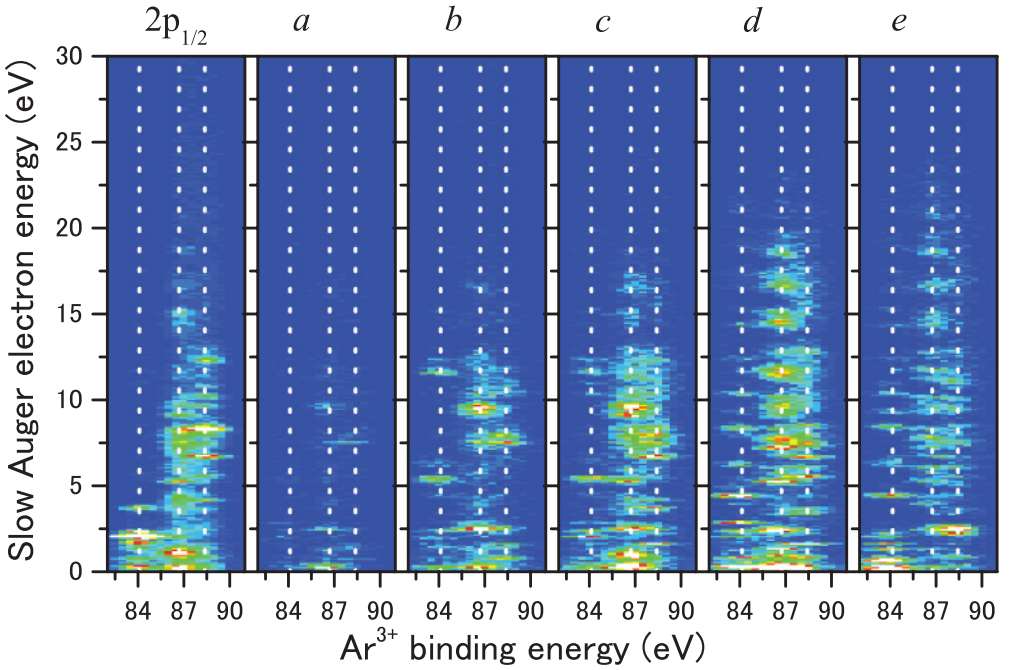

FIG. 4. (Color online) Two-dimensional Auger spectra associated with the double Auger decay of $Ar^+(2p_{1/2}^{-1})$ and $Ar^+(2p^{-1}3p^{-1}np)$ satellite states. They are obtained by coincidences between the photoelectron and the two Auger electrons, and represented as a function of the binding energy of the $Ar^{3+}(3p^{-3})$ final state (x axis) and the slower Auger electron energy (y axis). The Ar^{3+} binding energy $E_{B^{3+}}$ is deduced from the relation $E_{B^{3+}} = h\nu - (E_{\rm ph} + E_{A1} + E_{A2})$, where $E_{\rm ph}$ is the photoelectron energy and E_{A1} and E_{A2} are the Auger electron energies. The dotted vertical lines indicate the binding energies of the $Ar^{3+}(3p^{-3})$ states (^4S: 84.124 eV, ^2D: 86.7 eV, ^2P: 88.4 eV [28]). Since $E/\Delta E = 60$, the resolution of the horizontal axis (faster Auger electron) is less than that of the vertical axis (slower Auger electrons).

The peaks originating from the participator decay to the $Ar^{2+}(3p^{-2})$ or $Ar^{2+}(3s^{-1}3p^{-1})$ states also appear in Fig. 3(b), although their intensities are much lower than those of the spectator decay process. The intensity of the participator decay in the e zone is much weaker than for the a–d ones, suggesting that the $Ar^+(2p^{-1}3p^{-1}np)$ states experience less frequently participator decay when n increases. A small contribution due to the valence double photoionization process is included in Fig. 3, as the weak diagonal lines are seen in Fig. 2(a).

Next, we discuss the double Auger decay from the $Ar^+(2p^{-1}3p^{-1}np)$ satellite states. In a double Auger decay process, two Auger electrons are emitted simultaneously or sequentially. In the former two Auger electrons share continuously the available energy, while in the latter an intermediate Ar^{2+*} state is populated in the first Auger decay and followed by emission of another electron in the second one.

Figure 4 shows the two-dimensional Auger spectra associated with the double Auger decay of $Ar^+(2p_{1/2}^{-1})$ and $Ar^+(2p^{-1}3p^{-1}np)$ satellite states. They are obtained from coincidence between the photoelectrons and two Auger electrons, and display the energy correlation between the two Auger electrons. More strictly, the horizontal axis represents the binding energy of Ar^{3+} final states, converted from the sum of the three electrons' energies, and the vertical axis the energy of the slower Auger electron. The energy resolution for the Ar^{3+} final states is sufficient to distinguish the fine structures of the ground $Ar^{3+}(3p^{-3})$ states, the locations of which are indicated by vertical dotted lines.

Many narrow horizontal structures appear on these maps. They originate from the sequential (cascade) double Auger processes, and the energies of the slower Auger electrons correspond to the second step Auger decay (autoionization) from the intermediate Ar^{2+*} states to the $Ar^{3+}(3p^{-3})$ levels. The structures observed in the decay for a–e differ from each other, which suggests that intermediate Ar^{2+*} states populated by the spectator Auger decay are dependent on the initial $Ar^+(2p^{-1}3p^{-1}np)$ states. The population of these intermediate Ar^{2+*} states is seen in Fig. 3 as the structures lying above the Ar^{3+} threshold. Most intermediate Ar^{2+*} states occurring in the corresponding range can be assigned to $Ar^{2+}(3s^{-1}3p^{-2}np)$. Contribution from the $Ar^{2+}(3p^{-3}np)$ states is also seen specially in the decay of the e range, and from Fig. 4 we can deduce that they autoionize into the $Ar^{3+}(3p^{-3}, {}^4S)$ ground state.

The indirect double Auger decay via the $Ar^{2+}(3p^{-4}3d^2)$ state to the $Ar^{3+}(3p^{-3}, {}^4S)$ state (with release of a 2.19 eV electron) was the strongest decay path in the decay of the $Ar^+(2p^{-1})$ states [15], and is confirmed here in Fig. 4, but this process does not appear in the decay of the $Ar^+(2p^{-1}3p^{-1}np)$ satellite states.

Although direct double Auger process should appear as a continuous structure, it is almost invisible in our observations. Thus, the indirect double Auger process is the dominant process in the double Auger decay of Ar^{+*} satellite states, which can be compared to the decay process of the Ne 1s hole and the satellite states [5].

Figures 5(a) and 5(b) show the Ar^{3+} states created by double Auger decay of $Ar^+(2p^{-1})$ and $Ar^+(2p^{-1}3p^{-1}np)$

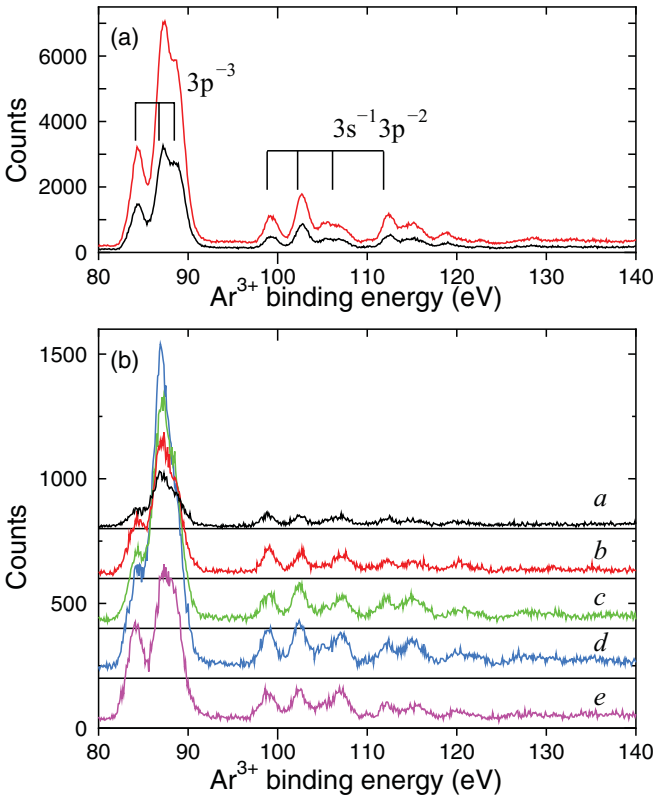

FIG. 5. (Color online) (a) Binding energy of the Ar^{3+} states created by double Auger decay of the $Ar^{+}(2p^{-1})$ states. They are obtained by coincidence between the corresponding photoelectron and two Auger electrons. The vertical bars indicate the binding energies of $Ar^{3+}(3p^{-3}$: ^4S, ^2D, and $^2P)$ and $Ar^{3+}(3s^{-1}3p^{-2}$: ^4P, ^2D, ^2S, and $^2P)$ states [28]. (b) Binding energy of the Ar^{3+} states created by double Auger decay of $Ar^{+}(2p^{-1}3p^{-1}np)$ states. The legends are the same as Fig. 3. To see easily, each base line is shifted by 200.

satellite states, respectively. The peaks in the 80–90 eV range correspond to $Ar^{3+}(3p^{-3})$ final states, and the peaks around 100–120 eV to $Ar^{3+}(3s^{-1}3p^{-2})$ states. This figure shows that the $Ar^{+}(2p^{-1}3p^{-1}np)$ states as well as $Ar^{+}(2p^{-1})$ states populate preferentially $Ar^{3+}(3p^{-3})$ final states in the double Auger decay. This is in contrast to the distributions of the Ar^{2+} states in single Auger decay that differ greatly between $Ar^{+}(2p^{-1})$ and $Ar^{+}(2p^{-1}3p^{-1}np)$ states as shown in Fig. 3. The relative populations of the final Ar^{3+} states by double Auger decay from $Ar^{+}(2p^{-1})$ and $Ar^{+}(2p^{-1}3p^{-1}np)$ states look rather similar although the decay paths are different as discussed above.

There is no clear evidence above 120 eV for the decay of $Ar^{+}(2p^{-1}3p^{-1}np)$ states to $Ar^{3+}(3p^{-4}np)$ states, where the np electron would remain as spectator. It appears hence that the excited np electron that remains as spectator in the first step of the Auger decay is finally ejected in the second step by an autoionization process involving reorganization of the Ar^{3+} core.

The probability for a 2p core hole or a 2p satellite state to experience a double Auger decay can be estimated from the ratio of the coincidences involving one or two Auger electrons from Figs. 3 and 5, respectively. Taking into account the electron detection efficiency we obtain probabilities of 15% and 21% for the 2p core hole or the 2p satellite states, respectively. The former is essentially in agreement with the previous measurements [15,27].

B. Auger decay of the $Ar^{+}(2p^{-1}3s^{-1}4s)$ states

The main difference between the $Ar^{+}(2p^{-1}3s^{-1}4s)$ and $Ar^{+}(2p^{-1}3p^{-1}np)$ satellite states arises from the fact that the $Ar^{2+}(2p^{-1}3p^{-1})$ states are energetically accessible to Auger decay from $Ar^{+}(2p^{-1}3s^{-1}4s)$ satellite state (see Fig. 1). Our results demonstrate that the $Ar^{+}(2p^{-1}3s^{-1}4s)$ satellite states decay first to the $Ar^{2+}(2p^{-1}3p^{-1})$ states. Figure 6(b) shows a two-dimensional map of the electron energy correlations. It is a zoom on the lower part of Fig. 2(a), where the energy range is selected to show the core-valence double ionization process to $Ar^{2+}(2p^{-1}3p^{-1})$ states. Figure 6(a) shows the photoelectron spectrum, in which the two peaks are assigned to $Ar^{+}(2p^{-1}3s^{-1}4s)$ states. On the diagonal structures corresponding to the double ionization to the $Ar^{2+}(2p^{-1}3p^{-1})$ states, there are enhanced structures when the faster electron energy is equal to the photoelectron energies of the $Ar^{+}(2p^{-1}3s^{-1}4s)$ satellite states. This indicates that the $Ar^{+}(2p^{-1}3s^{-1}4s)$ states decay to the $Ar^{2+}(2p^{-1}3p^{-1})$ states, where the 3s hole is filled first. On the other hand, in the case of the 2p hole being filled first, the participator decays from the $Ar^{+}(2p^{-1}3s^{-1}4s)$ states should populate the $Ar^{2+}(3s^{-1}3p^{-1})$ or $Ar^{2+}(3s^{-2})$ states, and the spectator decays the $Ar^{2+}(3s^{-1}3p^{-2}4s)$ or $Ar^{2+}(3s^{-2}3p^{-1}4s)$ states. However, these are minor processes, as shown in Fig. 2(a), where the relevant structures are hardly discernible on the diagonal lines corresponding to the formation of these Ar^{2+} states. Actually, the experimental data show that the probability of the decay of a 2p hole being formed prior to the 3s hole is around 17%. Theoretical calculations also indicate that the $Ar^{+}(2p^{-1}3s^{-1}4s)$ states do not undergo decay of the 2p hole, but decay with a strong selectivity to the $Ar^{2+}(2p^{-1}3p^{-1})$ states. Note that this observation is in contrast with the decay of the $Ar^{+}(2p^{-1}3p^{-1}np)$ states where it is the 2p hole which is filled first.

The spectroscopy of the $Ar^{2+}(2p^{-1}3p^{-1})$ $^{2S+1}L_J$ states is known [16] and Fig. 6(b) demonstrates that the different $^{2S+1}L_J$ components are partly resolved in the present experiment. Figure 6(c) shows the faster electron spectra emitted by double photoionization to the $Ar^{2+}(2p^{-1}3p^{-1})$ $^{2S+1}L_J$ states. These are obtained by the projection of the corresponding diagonal line into the horizontal axis. It is seen that the peak structures of the sequential double photoionization via the $Ar^{+}(2p^{-1}3s^{-1}4s)$ satellite states are superimposed on the flat structure due to the direct core-valence double photoionization (3p shake-off process in 2p photoionization). It is clear that the decay pattern of the $Ar^{+}(2p^{-1}3s^{-1}4s)$ states is dependent of the fine structure components and even presents a strong selectivity. Note that the decay of the Ar^{+} $2p^{-1}(^2P_{3/2})3s^{-1}4s$ states to the $Ar^{2+}(2p^{-1}3p^{-1})$ $^1S_0$ state is energetically forbidden.

Figure 7 shows the relative intensities of the decays from the $Ar^{+}(2p^{-1}3s^{-1}4s)$ states to the $Ar^{2+}(2p^{-1}3p^{-1})$ states obtained by estimating the area of each peak of Fig. 6(c). Figure 7(a) shows the decay from the $2p^{-1}(^2P_{3/2})3s^{-1}4s$ states (the lower binding energy peak) and Fig. 7(b) the

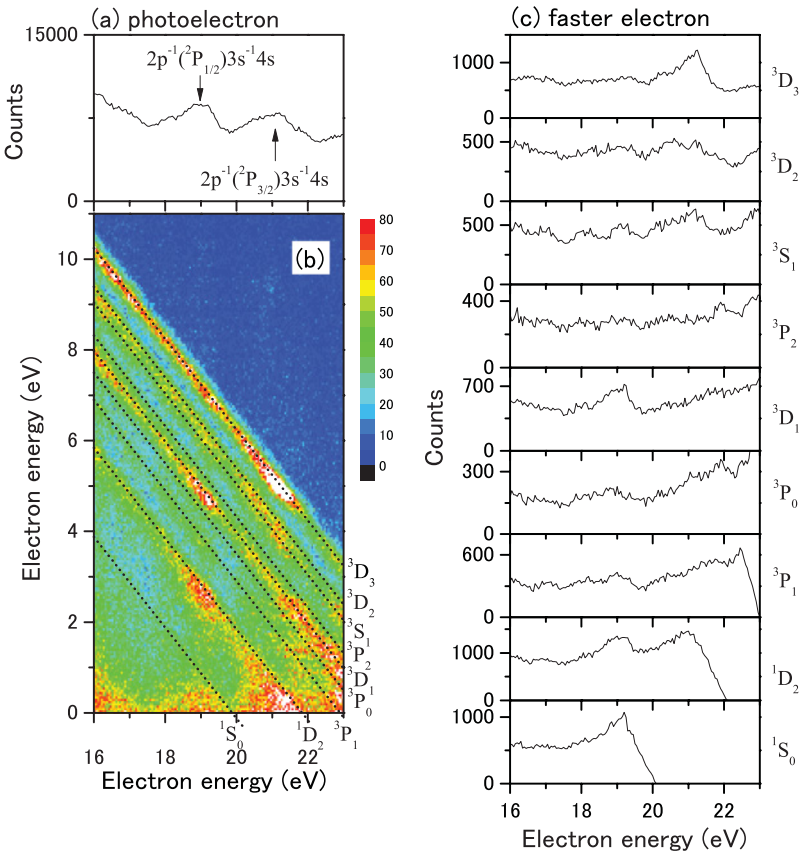

FIG. 6. (Color online) (a) Photoelectron spectrum. (b) Two-dimensional map of all coincidence pairs represented as a function of the kinetic energies of two electrons. The diagonal lines correspond to the core-valence double ionization process populating $Ar^{2+}(2p^{-1}3p^{-1})$ $^{2S+1}L_J$ states; these term values are labeled in the figure. (c) Faster electron spectra of double photoionization to individual $Ar^{2+}(2p^{-1}3p^{-1})$ states obtained by the projection of the corresponding diagonal lines to the horizontal axis.

decay from the $2p^{-1}(^2P_{1/2})3s^{-1}4s$ states (the higher binding energy peak). It is seen that the $2p^{-1}(^2P_{3/2})3s^{-1}4s$ states tend to decay to the $^3D_3$, $^3D_2$, and $^3S_1$ states, and that the $2p^{-1}(^2P_{1/2})3s^{-1}4s$ states tend to decay preferentially to the $^3D_1$ and $^1D_2$ states. The calculations, also given in Fig. 7, support the observed selectivity. In the calculated distributions, the population of the fine structure components of the initial $2p^{-1}3s^{-1}4sL_J$ states is assumed to follow the statistical weight.

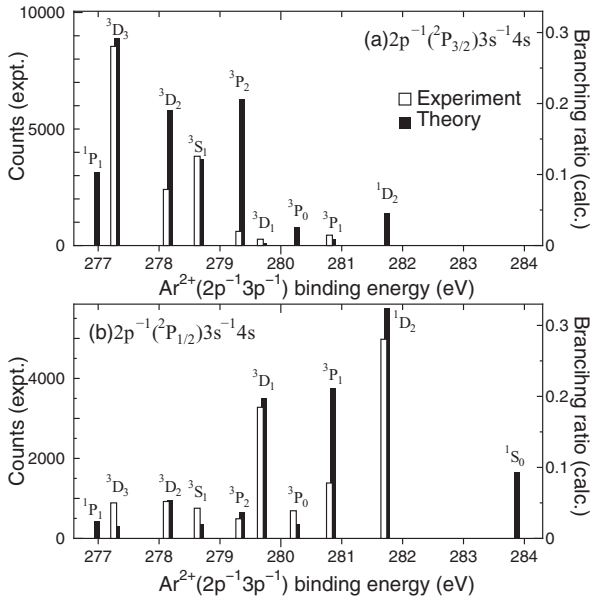

FIG. 7. Branching ratios for the decay from the $Ar^+(2p^{-1}3s^{-1}4s)$ states to the $Ar^{2+}(2p^{-1}3p^{-1})$ $^{2S+1}L_J$ states: (a) the decay from the $2p^{-1}(^2P_{3/2})3s^{-1}4s$ states, and (b) that from the $2p^{-1}(^2P_{1/2})3s^{-1}4s$ states. The white bars show the peak areas of each peaks observed in Fig. 6(c), the black bars are the calculated intensities.

These $Ar^{2+}(2p^{-1}3p^{-1})$ states decay subsequently mainly into $Ar^{3+}(3p^{-3})$ states, emitting an Auger electron around a kinetic energy of 190 eV. The corresponding structure can be seen on the 2D map in Fig. 2(a). The same $Ar^{2+}(2p^{-1}3p^{-1})$ states can be formed also in the Auger decay of the $Ar^+(2s^{-1})$ state, and their decay behavior is discussed in detail in Ref. [16].

V. CONCLUSION

In this work we have investigated the Auger decay of the Ar $2p$ hole and $2p$ satellite states. It is revealed that the main decay processes of the $Ar^+(2p^{-1}3p^{-1}np)$ and $Ar^+(2p^{-1}3s^{-1}4s)$ states are as follows:

$$Ar^+(2p^{-1}3p^{-1}np) \rightarrow Ar^{2+}(3p^{-3}np) + e$$

and

$$Ar^+(2p^{-1}3s^{-1}4s) \rightarrow Ar^{2+}(2p^{-1}3p^{-1}) + e,$$

respectively.

A valence electron fills first the $2p$ core hole in the decay of the $Ar^+(2p^{-1}3p^{-1}np)$ states while the np electron

remains mainly as spectator. On the other hand, the valence electron fills the $3s$ valence hole first in the decay of the $Ar^{+}(2p^{-1}3s^{-1}4s)$ state with emission of the $4s$ electron. For this state, with the opening of the decay channel to the $Ar^{2+}(2p^{-1}3p^{-1})$ states, the decay patterns drastically change.

ACKNOWLEDGMENTS

We warmly thank Ronald McCarroll for a critical reading of the manuscript. This work has been carried out under the support of the Photon Factory Program Advisory Committee for Proposals No. 2008G529 and No. 2010G610.

[1] W. E. Moddeman, T. A. Carlson, M. O. Krause, and B. P. Pullen, J. Chem. Phys. **55**, 2317 (1971).

[2] T. Kylli, H. Aksela, O. P. Sairanen, A. Hiltunen, and S. Aksela, J. Phys. B **30**, 3647 (1997).

[3] J. H. D. Eland, O. Vieuxmaire, T. Kinugawa, P. Lablanquie, R. I. Hall, and F. Penent, Phys. Rev. Lett. **90**, 053003 (2003).

[4] R. Kruit and F. H. Read, J. Phys. E **16**, 313 (1983).

[5] Y. Hikosaka, T. Aoto, P. Lablanquie, F. Penent, E. Shigemasa, and K. Ito, J. Phys. B **39**, 3457 (2006).

[6] T. Kaneyasu, Y. Hikosaka, E. Shigemasa, P. Lablanquie, F. Penent, and K. Ito, J. Phys. B **41**, 135101 (2008).

[7] E. Andersson, S. Fritzsche, P. Linusson, L. Hedin, J. H. D. Eland, J. E. Rubensson, L. Karlsson, and R. Feifel, Phys. Rev. A **82**, 043418 (2010).

[8] P. Linusson, S. Fritzsche, J. H. D. Eland, L. Hedin, L. Karlsson, and R. Feifel, Phys. Rev. A **83**, 023424 (2011).

[9] D. P. Spears, H. J. Fischbeck, and T. A. Carkson, Phys. Rev. A **9**, 1603 (1974).

[10] K. G. Dyall, F. P. Larkins, K. D. Bomben, and T. D. Thomas, J. Phys. B **14**, 2551 (1981).

[11] D. J. Bristow, J. S. Tse, and G. M. Bancroft, Phys. Rev. A **25**, 1 (1982).

[12] B. Eriksson, S. Svensson, N. Mårtensson, and U. Gelius, J. Phys. B **21**, 1371 (1988).

[13] T. Hayaishi, E. Murakami, Y. Morioka, H. Aksela, S. Aksela, E. Shigemasa, and A. Yagishita, J. Phys. B **25**, 4119 (1992).

[14] L. Avaldi, G. Dawber, R. Camilloni, G. C. King, M. Roper, M. R. F. Siggel, G. Stefani, and M. Zitnik, J. Phys. B **27**, 3953 (1994).

[15] P. Lablanquie, L. Andric, J. Palaudoux, U. Becker, M. Braune, J. Viefhaus, J. E. D. Eland, and F. Penent, J. Electron Spectrosc. **156–158**, 51 (2007).

[16] P. Lablanquie, S.-M. Huttula, M. Huttula, L. Andric, J. Palaudoux, J. H. D. Eland, Y. Hikosaka, E. Shigemasa, K. Ito, and F. Penent, Phys. Chem. Chem. Phys. **13**, 18355 (2011).

[17] K. Amemiya, A. Toyoshima, T. Kikuchi, T. Kosuge, K. Nigorikawa, R. Sumii, and K. Ito, AIP Conf. Proc. **1234**, 295 (2010).

[18] K. Ito, F. Penent, Y. Hikosaka, E. Shigemasa, I. H. Suzuki, J. H. D. Eland, and P. Lablanquie, Rev. Sci. Instrum. **80**, 123101 (2009).

[19] M. Y. Kuchev and S. A. Sheĭnerman, Sov. Phys. JETP **63**, 986 (1986).

[20] G. B. Armen, J. Tulkki, T. Åberg, and B. Crasemann, Phys. Rev. A **36**, 5606 (1987).

[21] F. A. Parpia, C. F. Fisher, and I. P. Grant, Comput. Phys. Commun. **94**, 249 (1996).

[22] S. Fritzsche, J. Electron Spectrosc. **114–116**, 1155 (2001).

[23] G. Gaigalas, T. Zalandauskas, and S. Fritzsche, Compt. Phys. Commun. **157**, 239 (2004).

[24] S. Fritzsche, J. Nikkinen, S.-M. Huttula, H. Aksela, M. Huttula, and S. Aksela, Phys. Rev. A **75**, 012501 (2007).

[25] P. Glans, R. E. LaVilla, M. Ohno, S. Svensson, G. Bray, N. Wassdahl, and J. Nordgren, Phys. Rev. A **47**, 1539 (1993).

[26] G. C. King, M. Tronc, F. H. Read, and R. C. Bradford, J. Phys. B **10**, 2479 (1977).

[27] S. Brünken, C. Gerth, B. Kanngießer, T. Luhmann, M. Richter, and P. Zimmermann, Phys. Rev. A **65**, 042708 (2002).

[28] *NIST atomic spectra database* [http://physics.nist.gov/asd].